Design optimization of a Digital Tracking Calorimeter for proton CT purposes

H. E. S. Pettersen[1,2*], I. Meric[3], O. H. Odland[1], J. R. Sølie[3], D. Röhrich[2]

[a]*Department of Oncology and Medical Physics, Haukeland University Hospital, Norway*
[b]*Department of Physics and Technology, University of Bergen, Norway*
[d]*Department of Electrical Engineering, Western Norway University of Applied Sciences, Norway*

**Corresponding author: helge.pettersen@helse-bergen.no*

INSERT PAGE BREAK HERE

Abstract

Max 300 ord

1 Introduction

This should be concise and describe the nature of the problem under investigation and its background. It should also set your work in the context of previous research, citing relevant references. Introductions should expand on highly specialised terms and abbreviations used in the article to make it accessible for readers.

This introductory text is copied directly from the PTCOG poster abstract, and should be revised.

The Bergen Proton CT group has for a time been working with benchmarking a proof-of-concept Digital Tracking Calorimeter (DTC) assembly for use as a tracking calorimeter in a proton CT setup. The proof-of-concept DTC consists of 24 Monolithic Active Pixel Sensor layers interleaved with tungsten absorbers, originally built for the reconstruction of electromagnetic showers induced by gamma radiation in high energy physics experiments. As such, the original design does not reflect the requirements of a proton CT calorimeter, regarding precision measurements of the ranges of protons with energies up to 250 MeV. The next prototype of our DTC, optimized for use in a proton CT setup, is currently in a design optimization phase where iterations of the design is assisted by Monte Carlo simulations. The results from this work will provide valuable input to the final design optimization process.

Should include (Lee et al. 2016)!

2 Methods

The goal of this study is to optimize the geometrical and material design of the DTC. The target for such a design is the simultaneous optimization of the following metrics: high accuracy of the range determination, limited by a non-existent systematic bias; low uncertainty (standard deviation) in the range determination, limited by the proton beam's range straggling; high track reconstruction efficiency, i.e. the ability to disentangle and reconstruct all the protons in a single readout frame; and secondary constraints such as economy (number of layers), cooling and mechanical stability.

The range accuracy ensures that the patient's Stopping Power Ratio map is correctly identified, while a high range uncertainty and an efficient track reconstruction enables that fewer protons are needed during the scan, i.e. a lower dose to the patient and a faster scan time.

The following section will describe the analysis needed to obtain the accuracy, uncertainty and efficiency as introduced above. In short, a water phantom of variable thickness is used for degrading the beam to different energies. Each primary proton is tracked through the detector and its most likely Bragg Curve is found. The range accuracy is then calculated from the spread of the resulting Bragg Peak depth distribution, and is compared for the different geometries under study.

Note that in order to obtain the best possible estimates of the performance of the different DTC designs, the different parts of the analysis are treated separately: The track reconstruction step is omitted during the evaluation of the residual range calculation, where the tracks are obtained directly from the MC truth.

2.1 Monte Carlo simulations and geometry input files

In this study, the MC software GATE version 7.2 has been applied, together with the physics builder list QGSP_BIC_EMY, using default settings for step length and particle threshold (Grevillot et al. 2010). The mean ionization potential for water is set to 75 eV in order to facilitate comparisons with the PSTAR database (Berger et al. 2005).

Several geometrical configurations are needed to evaluate how the desired detector metrics: such as range accuracy, range uncertainty and track reconstruction efficiency, depends on the design. It is possible to define a large number of potential designs for the DTC, and some constraints must be put on the degrees of freedom. A baseline design based upon the original prototype of the DTC (Pettersen et al. 2017) is shown in **Figure 1**: While the geometry of the sensor chips and electronical components are kept, the energy degrading part of the sampling calorimeter, here called the *absorbers*, are chosen to be between 2 mm and 6 mm of either aluminum or carbon. The proposed design use an upgraded sensor chip compared to the original prototype, and as such the detector thickness might be decreased.

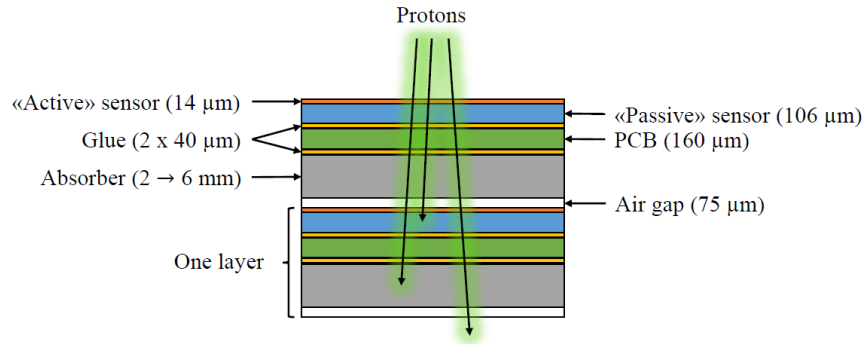

Figure 1: *Design to be optimized: Different thicknesses (2 to 6 mm) and materials (aluminum and carbon) for the energy absorbers are considered, and evaluated through the MC simulations. Only the "active" sensor part is readout in the MC simulations.*

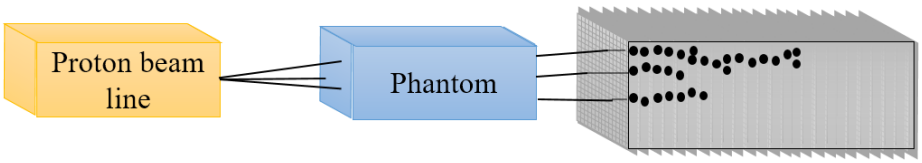

Figure 2: *Schematic setup of the variable geometry used for the design optimization. In order to obtain a spectrum of different proton beams to hit the DTC, the thickness of the energy degrading water phantom is modulated from 0 cm to the maximum range of the 250 MeV beam, which is approximately 38 cm.*

When the GATE software has been configured for a single geometry configuration, a number of scenarios are defined by varying the thickness of an energy degrading water phantom. By performing this step, a monoenergetic 250 MeV beam is modulated as to represent realistic energy spectra with

residual ranges that span the complete DTC in depth. The water phantom thicknesses vary from 0 cm to the maximum water equivalent range of the beam, approximately 38 cm, in steps of 1 mm. This fine thickness segmentation has been chosen in order to characterize the linearity of the range determination accuracy. The beam is placed distal to the water phantom, uniformly distributed from a plane, with an area of 100 cm^2, parallel to the sensor area. In **Figure 2** the placement of the water phantom is shown.

2.2 Proton range from Monte Carlo truth

The final range calculations that emerge from the following sections need to be compared to a ground truth, in this separate MC simulations are made for this purpose. A look-up-table between phantom thicknesses and residual DTC range is created, by using the geometrical input file as described above and recording the interactions in all volumes. This is repeated for all design variants and water phantom thicknesses. The look-up-table is then used in conjunction with spline interpolation, as this method is very accurate (Pettersen et al., n.d.).

A look-up-table for proton ranges in pure water is also created in order to calculate the Water Equivalent Thickness from a given proton range in the DTC: This is done by calculating the energy from the proton range, and then the WET from the energy. Note that this procedure is more accurate compared to using a constant stopping power ratio between water and the detector materials.

2.3 Track reconstruction

One of the strengths of the DTC design is its ability to untangle and reconstruct a large number of concurrent traversing proton tracks. To this end, a track reconstruction algorithm must be defined. For more details on the track reconstruction applied in this context, see (Pettersen et al. 2017).

2.3.1 Track-following scheme

The track reconstruction is based upon a track-following scheme (Strandlie and Frühwirth 2010). A *hit* is here defined to be a single, or a cluster of, pixels activated by a traversing proton. A *track* is a collection of hits, and should represent the path of the original proton. The track-following scheme is then: For a given hit in the first layer of the DTC, the angular change θ (assuming a parallel incoming proton) is calculated for all hits in the next layer. If the angular change is smaller than a reference value $f_i\theta_R$, the hit is appended to the growing track. The procedure in then continued until no more hits can be found to be appended to the growing track. The value θ_R is defined as the "3σ" value of the angular change distribution in the tracks obtained from the MC truth. The track-following scheme is performed two consecutive times using different values for f_i: $f_1 = 2$ and $f_2 = 3$. Due to the fact that the tracks have a higher scattering power towards the Bragg Peak, the track reconstruction is performed two more times starting at the last identified hit towards the Bragg Peak: This time the values $f_3 = 5$ and $f_4 = 7$ are chosen as to include proton paths with high amounts of scattering.

2.3.2 The correctly reconstructed track

In order to benchmark the quality and efficiency of the track reconstruction algorithm as described above, a definition of the correctly reconstructed track must be made. The constraints are therefore: The first and last entry in a track must originate from the same proton history, and the last hit from a proton history must be included. By following this definition, the track objects have correct incoming vector and residual range, which is the required values for volumetric reconstruction of the stopping power map in proton CT.

The efficiency of the track reconstruction is then the ratio of correctly reconstructed tracks to the total number of identified tracks. Tracks stopping due to inelastic collisions do not degrade the efficiency; they can be identified due to a lack of an increase in the deposited energy at the distal part of the track due from the Bragg Peak. The efficiency is found for an increasing number of protons reconstructed simultaneously.

2.4 Bragg Curve fitting

It is possible to perform least-square fits of the Bragg Curve to the track's energy loss measurements in each sensor layer. This procedure increases the range determination accuracy compared to using the depth of the last recorded hit. While direct measurement of the energy loss is not possible using the proposed digital sensor readout ("hit" or "no hit"), it is possible to estimate the energy loss by counting the number of connected hits originating from the proton path, as described in detail in (Pettersen et al. 2017), and as such this kind of model fitting is performed.

2.5 Residual range and range straggling calculation

The distribution of true proton ranges, having the same initial energy, is approximately gaussian. However, the output range distribution originating from the Bragg Curve fitting is not gaussian, and it is not trivial to describe the variations analytically due to the nature of the spare measurements from each sensor layer. However, a simple histogram calculation of the empirical mean value and standard deviation yields accurate results for the residual range $\langle R_0 \rangle$ and range straggling $\langle \sigma \rangle$, respectively. The procedure is described in detail in (Pettersen et al. 2017): A gaussian fit (μ', σ') to the whole range distribution histogram with weights w_i and depth values x_i yields the summation limits for the bin counting from $x_1 = \mu' - 4\sigma'$ to $x_2 = \mu' + 4\sigma'$. Then,

$$\langle R_0 \rangle = \frac{\sum_{i=x_1}^{x_2} w_i x_i}{\sum_{i=x_1}^{x_2} w_i}, \qquad \langle \sigma \rangle = \sqrt{\frac{\sum_{i=x_1}^{x_2} w_i (x_i - \langle R_0 \rangle)^2}{\left[\sum_{i=x_1}^{x_2} w_i\right] - 1}}.$$

The results of these calculations should be comparable to the ground truth obtained from separate MC simulations. However, it is expected that the values should be degraded somewhat. First, in terms of a systematic error, or bias, leading to deviations in $\langle R_0 \rangle$ compared to the nominal residual range. Second, in terms of an increase in the measurement uncertainty $\langle \sigma \rangle$ compared to the range straggling. These degradations may originate from the design of the DTC setup and from how the data analysis is performed. By comparing the measured values to their ground truth counterparts, the bias in $\langle R_0 \rangle$ is trivial to calculate in different phase space scenarios.

3 Results

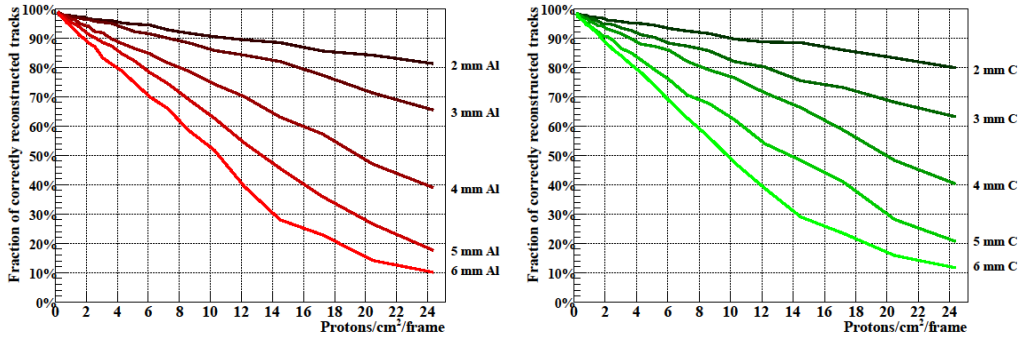

Figure 3: *The tracking efficiency for different geometries. Each proton track must be fully reconstructed, and the start- and endpoint must originate from the same incoming proton. The results from the designs using aluminum and carbon absorbers are similar. Note that in many cases, the effect of a wrongly reconstructed track might be small due to the nature of the error: Parallel tracks originating from similar incoming vectors are easily confused.*

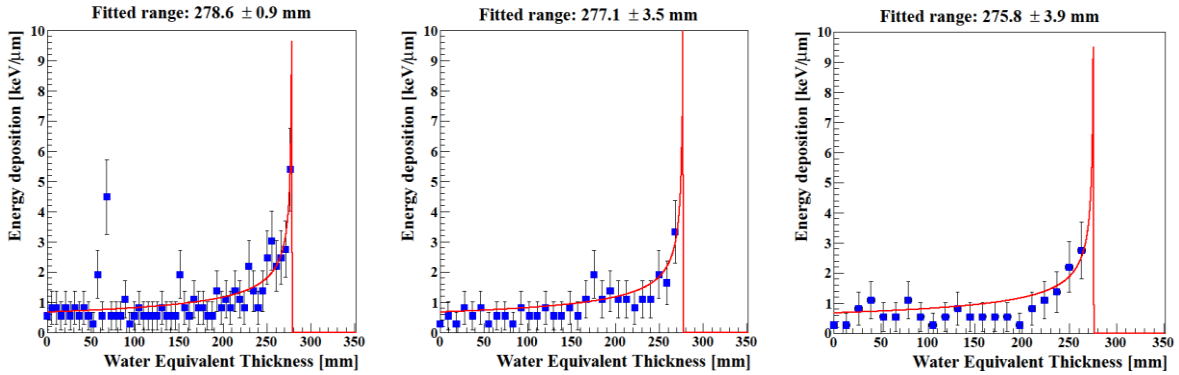

Figure 4: *Individual proton tracks with Bragg Curve fit. Note that the range found using thinner absorber designs yields a higher range determination accuracy. The displayed accuracy is the output from the least-square method for an individual proton, and is not representative for an ensemble of protons. From a 250 MeV beam degraded using a 10 cm water phantom.* ***Left****: 2 mm Al absorber,* ***Middle****: 4 mm Al absorber,* ***Right****: 6 mm Al absorber.*

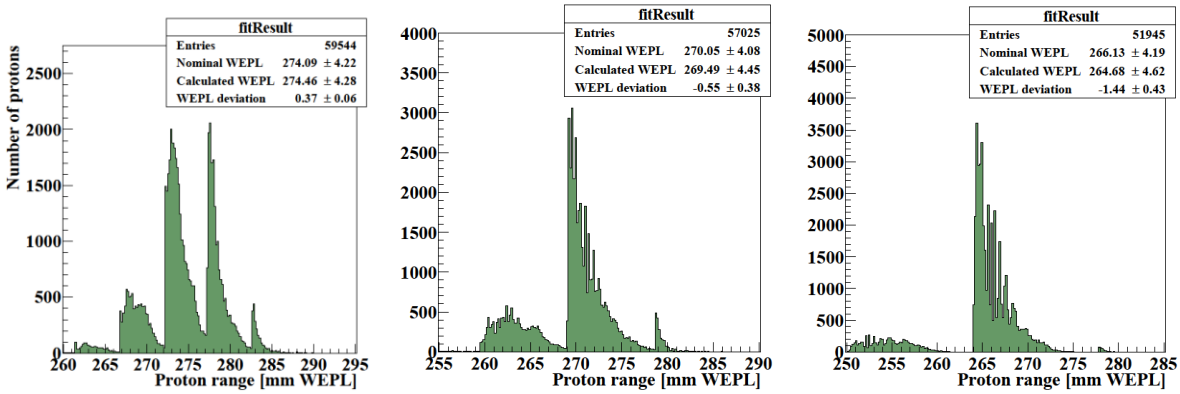

Figure 5: *The distribution of many individual fitted ranges. From this distribution the residual range* $\langle \boldsymbol{R_0} \rangle$ *and range straggling* $\langle \boldsymbol{\sigma} \rangle$ *of a proton ensemble is calculated, shown here as* $\langle \boldsymbol{R_0} \rangle \pm \langle \boldsymbol{\sigma} \rangle$*. Each rise in the distribution coincides with the beam reaching a new sensor layer. From a 250 MeV beam degraded using a 10 cm water phantom.* ***Left****: 2 mm Al absorber,* ***Middle****: 4 mm Al absorber,* ***Right****: 6 mm Al absorber.*

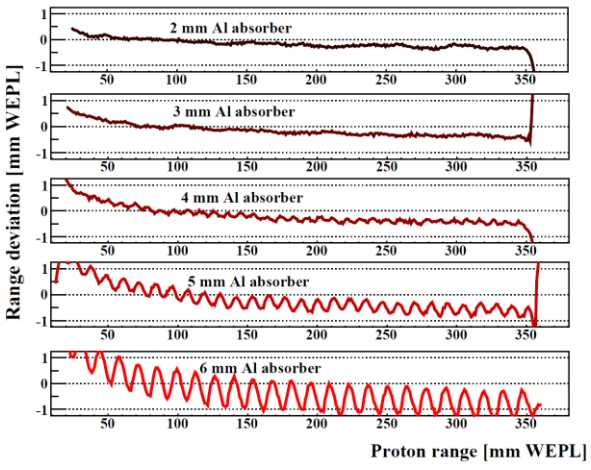

Figure 6: *Range determination accuracy shown as the deviation between the true (MC) range, and the reconstructed range* $\langle \boldsymbol{R_0} \rangle$ *for each water degrader thickness. In general the systematic errors are kept within 0.5 mm WET. An oscillating systematic error occurs when using thick absorbers due to the large spacing between the measurements in subsequent layers. TO BE UPDATED*

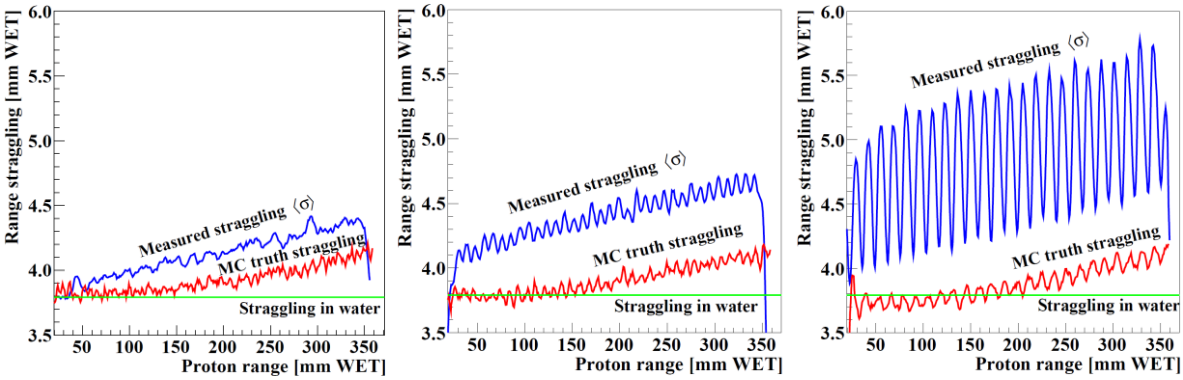

Figure 7: *The measured range straggling ⟨σ⟩, shown here together with the MC truth range straggling and the "baseline" range straggling in water. An oscillating systematic error occurs when using thick absorbers due to the large spacing between the measurements in subsequent layers.* ***Left:*** *2 mm Al absorber,* ***Middle:*** *4 mm Al absorber,* ***Right:*** *6 mm Al absorber. TO BE UPDATED*

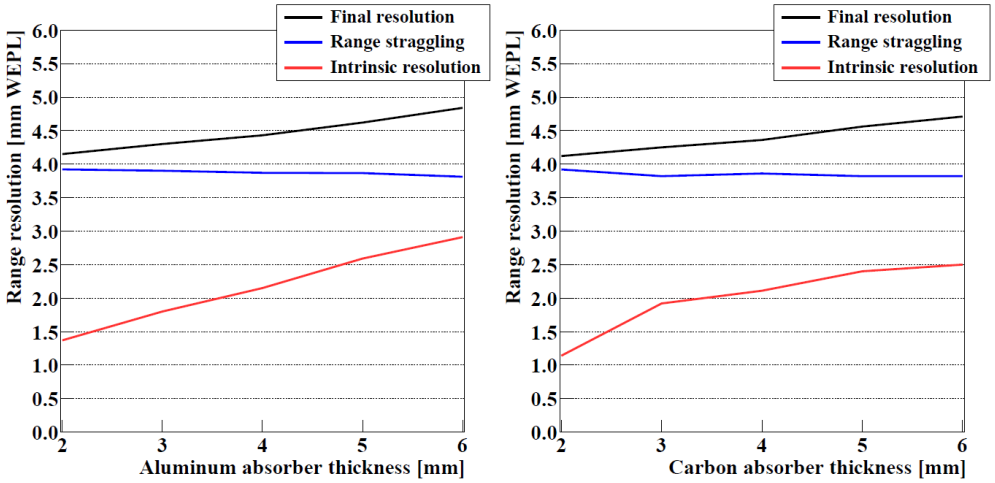

Figure 8: *Range resolution of the different configurations. Shown is the total resolution (measured as the mean value of* ***⟨σ⟩*** *in* ***Figure 6****), the range straggling from the MC truth as well as the intrinsic resolution which is the quadratic difference between the two. TO BE UPDATED. SWITCH COLORS: <S> SHOULD BE BLUE TO MATCH FIGURE 7, RANGE STRAGGLING SHOLD BE RED!*

3.1 Efficiency of track reconstruction

The efficiency of the track reconstruction, as defined in Section 2.3.2, is shown in **Figure 3** for the 12 different designs under consideration. It is calculated using a 100 cm^2 irradiation field and by varying the number of protons reconstructed simultaneously. For the 4 mm design, both using aluminum and carbon, the efficiency is 90% at 4 protons per cm^2 per reconstruction frame, and 80% if the proton density is doubled.

3.2 Accuracy of the range calculation

In **Figure 6** the range determination accuracy throughout the DTC is shown for the different designs. Some key aspects can be seen in the figure: The *systematic errors* are kept within 0.5 mm WET throughout the DTC for the designs having a 4 mm Al absorber or less, and higher for the designs with more than 4 mm Al absorbers. The *dynamic range* of the DTC, given by the region with uniform range uncertainty and uniform range accuracy, is approximately between 20 mm WET and 350 mm WET in the detector, or in terms of energy between 50 MeV and 240 MeV. There is a certain oscillation artefact in the range determination to be observed, especially at the designs with more than 4 mm and thicker absorbers. It is characterized by a sinusoidal perturbation of the range accuracy due to the sparse sampling of the layer measurements in depth. A spectral analysis of the range accuracy has

shown that this oscillation becomes significant (having a peak-to-peak amplitude of more than 0.25 mm WET) when an aluminum absorber thickness above 4.5 mm is used.

3.3 Uncertainty of the range calculation

The uncertainty of the range determination is highly dependent on its lower limit, which is the statistical range straggling of the proton beam. The resulting range uncertainty is a quadratic sum between the range straggling and the additional smearing due to detector and analysis. As is apparent in **Figure 7**, the range straggling is dominated by the straggling induced by interactions in the water phantom, with an increase in the uncertainty for high energy protons traversing a higher fraction of the DTC material. The range straggling inhibits an oscillating systematic error with a period matching the spacing of the sensor layers, similar to the effects described in **Section 3.2**.

3.4 Comparison of different geometries

It is possible to calculate the "intrinsic" or additional uncertainty of the setup by subtracting the range straggling from the measured range spread $\langle\sigma\rangle$ in quadrature. In **Figure 8** the range straggling, intrinsic uncertainty as well as the total measured uncertainty of two designs are shown. SOME OF THE RESULTS HERE WHEN THEY ARRIVE.

3.5 Required number of sensor layers

Due to economical and size constraints, the number of layers required to contain the complete beam has been found for the different designs. A 230 MeV mono-energetic beam has been considered here, its range plus 5 times the range straggling leads to the following number of layers: For the 2 mm configuration, 67 layers are needed. For 3 mm, 49 layers are needed. For 4 mm, 38 layers are needed. Only 32 (27) layers are needed for the 5 (6) mm configuration, although it has been shown that these designs lead to excessive range determination errors.

4 Discussion

This should discuss the significance of the results and compare them with previous work using relevant references.

The design, analysis framework and capabilities of the original DTC were detailed in (Pettersen et al. 2017). Among its key features are a "all-in-one" design where the entrance of the calorimeters can double as the proton tracker and a high rate capability due to the possibility of the tracking and reconstruction of hundreds of simultaneous proton tracks. The calorimeter performed above expectations but did not meet the requirements for a proton CT calorimeter as suggested in (Poludniowski, Allinson, and Evans 2015). Its main limitation for proton CT purposes were shown to be the utilization of 3.3 mm tungsten absorbers between each sensor layer, roughly equivalent to 15.5 mm aluminum. The resulting range uncertainty for both experimental data and MC simulations was above 8 mm WET in addition to oscillating systematic errors of up to 8 mm.

The next generation DTC, as described in this study, is designed with proton CT as the main purpose. While the analysis framework and design philosophy remains, energy absorbers of less dense materials facilitate the track reconstruction as well as the range calculation. A comparison of the results presented here to the results of the original prototype shows that both systematic errors and range uncertainties are close to their theoretical limits of, respectively, zero and the inherent range straggling for several of the proposed designs. These capabilities are matched by current proton CT prototypes based on staged scintillators (Bashkirov et al. 2016) and parallel plate ionization chambers (Rinaldi et al. 2014).

This analysis was performed on a water phantom of varying thickness, however it is trivial to extend it to realistic phantoms since the incoming proton vector is well defined by the first two layers of the DTC, which are defined without the absorber material: Reducing the beam energy by less than 0.5

MeV. In terms of cooling and mechanical stability, a 4 mm aluminum absorber should provide the required support, and increasing air gap of 2 mm might enable an air-cooled design.

Using realistic assumptions about the geometry (350 cm^2) and electronics capabilities (10 µs readout cycle) of the DTC design under consideration, and under the assumption that a large-area proton irradiation field can be delivered, this proton density corresponding to a 90% reconstruction efficiency converts to a proton rate capability of the DTC of 140 million protons per second. This number is above the minimum requirements of a proton CT, and of current prototypes (Scaringella et al. 2014; Bashkirov et al. 2016; Taylor et al. 2016; Naimuddin et al. 2016), and may enable scan times limited by gantry rotation speeds.

Another use case of such a readout scheme is the reconstruction of thousands of almost coincident protons, such as protons accelerated by the proposed Laser Accelerated Proton methods (Masood et al. 2014; Hofmann et al. 2015). If a large-area irradiation field is not available or not desired (e.g. by omitting the proximal tracker and using a thin pencil beam in order to simplify the design (K. M. Hanson et al. 1978)), the rate capability will decrease.

5 Conclusion

This section should be used to highlight the novelty and significance of the work, and any plans for future relevant work.

In this work we have benchmarked different designs of the next generation Digital Tracking Calorimeter (DTC) using MC simulations together with the analysis framework developed for the proof-of-concept DTC prototype (Pettersen et al. 2017).

The analysis is performed by combining individual proton tracking in a high-granularity pixel range telescope and Bragg Curve modeling of each proton's energy loss. The DTC has the capability of tracking more than 100 million protons/s at 90% reconstruction efficiency, assuming realistic electronics- and design proposals as well as a uniform large-area proton field. The range uncertainties are close to the range straggling limit, and systematic errors in the range determination are kept below 0.3 mm WET throughout the complete detector.

By considering the presented results, the optimal design in terms of the systematic and stochastic errors is 4 mm, with similar results between carbon and aluminum. The improvement achieved by using 3 mm or less absorbers is negligent due to the inherent range straggling limit to the range uncertainty. Thicker absorbers, however, yield a systematic oscillating artefact in the range determination accuracy and at 5 mm and higher this effect is degrading. In terms of the reconstruction efficiency, the smaller absorber the better: The thickness should not be far above 3 mm in order to obtain the optimal efficiency. However, when considering the realistic construction constraints, a 4 mm absorber leads to far fewer required sensor layers compared to the 3 mm design, respectively 48 and 39 needed layers, which might be a deciding factor between the two near-optimal alternatives.

This work provides input to the design of the next generation DTC in a proton CT setting, to be constructed by the Bergen Proton CT group. In addition, the Bragg Peak-guided range reconstruction presented here and in (Pettersen et al. 2017) might be of interest to similar projects.

6 Acknowledgements

This work was supported by Helse Vest RHF grant [911933], and is part of the main author's PhD project.

7 References

Bashkirov, V. A., R. W. Schulte, R. F. Hurley, R. P. Johnson, H. F.-W. Sadrozinski, A. Zatserklyaniy, T. Plautz, and V. Giacometti. 2016. "Novel Scintillation Detector Design and Performance for Proton Radiography and Computed Tomography." *Medical Physics* 43 (2): 664–74. doi:10.1118/1.4939255.

Berger, M. J., J.S. Coursey, M.A. Zucker, and J. Chang. 2005. *ESTAR, PSTAR, and ASTAR: Computer Programs for Calculating Stopping-Power and Range Tables for Electrons, Protons, and Helium Ions* (version 1.2.3). Gaithersburg, MD: National Institute of Standards and Technology. http://physics.nist.gov/Star.

Grevillot, Loïc, Thibault Frisson, Nabil Zahra, Damien Bertrand, Frédéric Stichelbaut, Nicolas Freud, and David Sarrut. 2010. "Optimization of GEANT4 Settings for Proton Pencil Beam Scanning Simulations Using GATE." *Nuclear Instruments and Methods in Physics Research Section B: Beam Interactions with Materials and Atoms* 268 (20): 3295–3305. doi:10.1016/j.nimb.2010.07.011.

Hofmann, Kerstin M., Umar Masood, Joerg Pawelke, and Jan J. Wilkens. 2015. "A Treatment Planning Study to Assess the Feasibility of Laser-Driven Proton Therapy Using a Compact Gantry Design." *Medical Physics* 42 (9): 5120–5129. doi:10.1118/1.4927717.

K. M. Hanson, J. N. Bradbury, T. M. Cannon, R. L. Hutson, D. B. Laubacher, R. Macek, M. A. Paciotti, and C. A. Taylor. 1978. "The Application of Protons to Computed Tomography." *IEEE Transactions on Nuclear Science* 25 (1): 657–60. doi:10.1109/TNS.1978.4329389.

Lee, Chae Young, Hankyeol Song, Chan Woo Park, Yong Hyun Chung, Jin Sung Kim, and Justin C. Park. 2016. "Optimization of Proton CT Detector System and Image Reconstruction Algorithm for On-Line Proton Therapy." Edited by Li Zeng. *PLOS ONE* 11 (5): e0156226. doi:10.1371/journal.pone.0156226.

Masood, U., M. Bussmann, T. E. Cowan, W. Enghardt, L. Karsch, F. Kroll, U. Schramm, and J. Pawelke. 2014. "A Compact Solution for Ion Beam Therapy with Laser Accelerated Protons." *Applied Physics B* 117 (1): 41–52. doi:10.1007/s00340-014-5796-z.

Naimuddin, Md, G. Coutrakon, G. Blazey, S. Boi, A. Dyshkant, B. Erdelyi, D. Hedin, et al. 2016. "Development of a Proton Computed Tomography Detector System." *Journal of Instrumentation* 11 (02): C02012.

Pettersen, H. E. S., M. Chaar, I. Meric, O. H. Odland, J. R. Sølie, and D. Röhrich. n.d. "Accuracy of Parameterized Proton Range Models; a Comparison." *Radiation Physics and Chemistry* Submitted.

Pettersen, H.E.S., J. Alme, A. Biegun, A. van den Brink, M. Chaar, D. Fehlker, I. Meric, et al. 2017. "Proton Tracking in a High-Granularity Digital Tracking Calorimeter for Proton CT Purposes." *Nuclear Instruments and Methods in Physics Research Section A: Accelerators, Spectrometers, Detectors and Associated Equipment* 860C: 51–61. doi:10.1016/j.nima.2017.02.007.

Poludniowski, G, N M Allinson, and P M Evans. 2015. "Proton Radiography and Tomography with Application to Proton Therapy." *The British Journal of Radiology* 88 (1053): 20150134. doi:10.1259/bjr.20150134.

Rinaldi, I, S Brons, O Jäkel, B Voss, and K Parodi. 2014. "A Method to Increase the Nominal Range Resolution of a Stack of Parallel-Plate Ionization Chambers." *Physics in Medicine and Biology* 59 (18): 5501–15. doi:10.1088/0031-9155/59/18/5501.

Scaringella, M, M Bruzzi, M Bucciolini, M Carpinelli, G A P Cirrone, C Civinini, G Cuttone, et al. 2014. "A Proton Computed Tomography Based Medical Imaging System." *Journal of Instrumentation* 9 (12): C12009–C12009. doi:10.1088/1748-0221/9/12/C12009.

Strandlie, Are, and Rudolf Frühwirth. 2010. "Track and Vertex Reconstruction: From Classical to Adaptive Methods." *Reviews of Modern Physics* 82 (2): 1419–58. doi:10.1103/RevModPhys.82.1419.

Taylor, J. T., G. Poludniowski, T. Price, C. Waltham, P. P. Allport, G. L. Casse, M. Esposito, et al. 2016. "An Experimental Demonstration of a New Type of Proton Computed Tomography Using a Novel Silicon Tracking Detector." *Medical Physics* 43 (11): 6129–6136.